Journal of the European Ceramic Society 44 (2024) 4294–4306

Contents lists available at ScienceDirect

Journal of the European Ceramic Society

journal homepage: www.elsevier.com/locate/jeurceramsoc

Effect of iron and organic matter on mineralogy and texture of replacement bricks for heritage conservation: The case of the Alhambra Formation soil (Granada, Spain)

Kerstin Elert *, Luis Monasterio-Guillot, Giuseppe Cultrone

University of Granada, Department of Mineralogy and Petrology, Fuentenueva S/N, 18071 Granada, Spain

ARTICLE INFO

Keywords:
Clay minerals
Mechanical resistance
Hydric behavior
Organic matter
Iron-oxyhydroxides
Oxidizing and reducing atmosphere

ABSTRACT

Throughout history, bricks have been an important part of monumental and vernacular architecture but often suffer alteration due to physico-chemical weathering and require replacement. Local soil could be used to fabricate compatible replacement bricks with similar physico-chemical characteristics as historic ceramics. Here the mineralogical and textural evolution of bricks prepared with local soil containing iron-oxyhydroxides and organic matter and fired between 800–1100 °C are evaluated. The study provides direct evidence for solid state formation of anorthite in contact with carbonate grains and sheds light on the fate of iron compounds under oxidizing and reducing conditions (induced by the presence of organic matter) and their influence on the textural evolution of fired bricks. Brick durability and compatibility are discussed based on their hydric and mechanical performance. The findings of this study further the understanding of temperature-induced soil mineral changes and have practical implications for the design of compatible bricks for heritage conservation and new construction.

1. Introduction

Bricks are one of the most widely used building materials; early use dating back as far as the Neolithic Daxi and Qujialing Cultures in China (5000–2600 BC [1]) and the Bronze Age Indus Valley Civilization (2600–1900 BC [2]). On Spanish territory, early brick use has been reported for the Roman site El Vila-sec (Tarragona) 50 BC – 150 AD [3] and they played a prominent role in the construction of the Alhambra fortress, a World Heritage site (Granada, Spain) (Fig. 1a and b), including the citadel, the palaces, the royal bath and the cemetery of the Nasrid period (13th −14th century AD) [4]. Since the 16th century, bricks also found broad application in the reconstruction of walls and towers at the Alhambra, including rammed earth structures (Fig. 1c) [5]. Today, it is common practice to recycle bricks during conservation interventions [6], but on occasions replacements are required when original bricks show poor quality and/or extensive degradation [7]. Replacement bricks have to fulfill basic compatibility requirements, which relate to their similarity in texture, hydric behavior and mechanical strength in order to avoid damage to the historic structure [8]. All these characteristics depend on raw clay composition and firing conditions but might change over time as degradation processes suffered by historic bricks often result in a decrease in strength and increase in porosity.

Here, we evaluate the suitability of local soil from the Alhambra Formation for the fabrication of bricks. The Alhambra fortress is built on this formation that is mainly composed of conglomerates. Previous studies have shown that Alhambra Formation soil was historically used as building material for rammed earth construction and as raw material for bricks [4,9,10], making it an interesting candidate for the fabrication of replacement bricks for local monuments. Considering that the soil of this study contains common soil minerals, findings will not only be of local interest but applicable to brick manufacturing and conservation interventions involving the replacement of bricks worldwide. Moreover, the soil includes oxyhydroxides and organic matter, which are typical in Mediterranean clayey soils. However, little is known regarding the combined effect of both components on the properties of fired bricks.

A wide array of analytical techniques and testing methods are employed in this investigation to perform a detailed study of the mineralogical evolution of the soil upon firing and its effect on the bricks' hydric, textural, and mechanical properties. The results obtained are contrasted with published data to determine the suitability of these bricks as replacement material in built heritage conservation,

* Corresponding author.
E-mail address: kelert@ugr.es (K. Elert).

https://doi.org/10.1016/j.jeurceramsoc.2024.01.062
Received 29 December 2023; Received in revised form 17 January 2024; Accepted 18 January 2024
Available online 20 January 2024

considering aspects related to compatibility and durability. Furthermore, the effect of the addition of a small amount of KOH (1 wt% based on soil dry weight) on the properties of fired bricks is evaluated in this study. Sodium and potassium salts, often in the form of plant ash, have historically been used as flux and relative high concentration of K_2O have been detected for example in the case of ancient glazed objects from Egypt and China (first millennium BC [11,12]). The outcome of this investigation not only furthers the understanding of temperature-induced soil mineral changes and historic ceramic technology, but also has significant implications in the design of compatible conservation materials and bricks for new construction.

2. Materials and methods

2.1. Sample preparation

For brick fabrication, soil from the Alhambra Formation was collected from the upper horizon of the hills near the Alhambra monument and the city of Granada (Southern Spain). The Alhambra Formation constitutes a good example of a fluvial (delta-fan) debris-flow deposit from the Pleistocene-Early Pliocene age, the reddish clay-rich material being typical of the Mediterranean region [13,14]). Large pebbles (>2 cm) were removed manually, and the soil was milled to obtain a material with suitable granulometry. According to the particle size measurement (Mastersizer 2000LF, Malvern Panalytical, UK) of an alcoholic dispersion, the soil mainly had particles in the range of 0.3 - 180 μm with the mean at 25 μm (Fig. 2). The milled soil also contained some larger grains, which were quantified by dry sieving (i.e., 13.4 wt

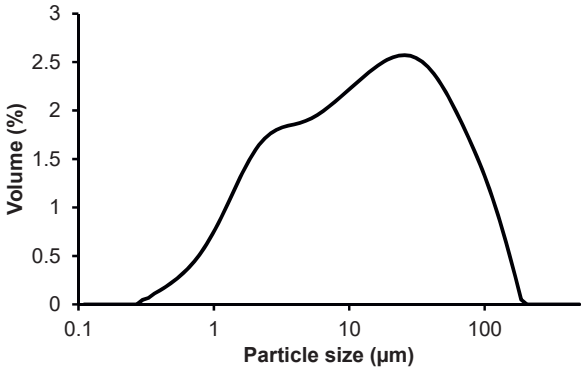

Fig. 2. Granulometry of the raw soil used for brick fabrication.

Fig. 1. Bricks of the Alhambra fortress (Granada, Spain). (a) General view of the "Puerta de la Justicia" (Gate of Justice), (b) detail of decorative masonry at the "Puerta de la Justicia" showing some material loss, and (c) historic reconstruction of the "Torre del Agua" (Water Tower, rammed earth structure) using bricks (white arrow).

% > 0.5 mm and 2.6 wt% > 1 mm).

Bricks were prepared with a 0.3 water/solid ratio using wooden frames (16 × 12 × 4 cm), which were filled with wet soil and compacted manually. The 0.3 water to solid ratio has been chosen as it produced clay putty of adequate consistency for manual brick fabrication. Atterberg limits were not determined. A second batch of bricks was prepared using the same mixing ratio but adding 1 wt% KOH (based on soil dry weight) as flux to the kneading water. KOH has been selected considering that sodium and potassium hydroxide are thought to be more efficient fluxes for lowering the melting temperature of silicate minerals as compared to their corresponding carbonates [15]. Higher efficiency can be explained by the simple fact that the same amount of metal hydroxide provides more potassium to the system than its carbonate (i.e, the potassium content of KOH and K_2CO_3 being 71 and 58 wt%, respectively). After 4 h, the green bricks were demolded and cut with a nylon thread into 4 × 4×4 cm cubes. The cubes were dried for 2 weeks in the laboratory (22 ± 3 °C and 45 ± 5% RH) prior to firing in a Herotec CR-35 electric oven at 800 °C, 950 °C and 1100 °C. Initially, T was kept constant at 100 °C for 1 h to eliminate any residual moisture from the samples. Subsequently, T was raised at 2 °C/min until the desired temperature was reached, which was kept constant for 3 h. Gradual heating at 2ºC/min was chosen based on previous experimental results, showing an adequate textural and phase evolution [8]. Upon completion of the firing process, bricks remained in the oven and cooled slowly during 24 h to prevent crack formation due to phase transition of β-to-α quartz. Once cold, bricks were immersed in water for 1 h in order to prevent possible "lime blowing" [16]. The sample acronyms for bricks fired at different T are A800, A950, and A1100R (outer red zone) A1100B (interior black zone) all without KOH, and AK800 and AK950, all with 1 wt% KOH.

2.2. Analytical methods and testing

Color parameters of green bodies and fired bricks were determined with a spectrophotometer (CM-700 d, Konika Minolta, Japan) using the CIE $L^*a^*b^*$ color space (i.e., L^* is lightness varying from black with a value of 0 to white with a value of 100; a^* and b^* are chromaticity coordinates, a^* varies from $+a^*$ (red) to $-a^*$ (green) and b^* from $+b^*$ (yellow) to $-b^*$ (blue)). Equipment settings were: illuminant D65, 10° viewing angle, 8 mm Ø aperture. Color change was calculated using the following formula: $\Delta E^* = (\Delta L^{*2} + \Delta a^{*2} + \Delta b^{*2})^{1/2}$. Average values are based on 10 measurements per sample.

To determine the mineralogical composition of the raw material and the phase evolution of the fired bricks, powder X-ray diffraction analysis (XRD, X'Pert PRO, Malvern Panalytical Ltd., UK) was performed using a crystalline internal standard (10 wt% corundum) for the subsequent quantification applying the Rietveld method [17]). Equipment settings: Cu-Kα radiation, Ni filter, 45 kV, 40 mA, 3–70°2θ scan range, 0.04°2θ step size, and 4 s per step. Mineral phase identification and quantification were performed using XPowder software [18] and the International Centre for Diffraction Data (ICDD) PDF-2 database, as well as HighScore Plus 2.2.4 (Malvern Panalytical Ltd., UK) and the American Mineralogist crystal structure database [19] for Rietveld analysis.

X-ray fluorescence (XRF) was employed to study the chemical composition (major elements) of the raw soil using a Zetium (Malvern Panalytical Ltd., UK) with an Rh anode and a 4 kV X-ray generator. The sample (5 g) was ground prior to analysis.

The Fe oxidation state of black and red areas of bricks fired at 1100 °C was determined with X-ray photoelectron spectroscopy (XPS) using an Axis Ultra-DLD (Kratos Analytical Ltd., U.K.) with monochromatic Al Kα radiation. Equipment settings: Survey spectra (2 scans) at 75 W x-ray source power and 160 eV pass energy, and high-resolution spectra (30 scans) of Fe 2p and Fe 3p at 225 W source power and 40 eV pass energy. The analyzed area was 300 × 700 μm in size. The C1s transition at 284.6 eV was used as reference. Data analysis was performed using CasaXPS software (Casa Software Ltd., UK).

Elemental analysis of nitrogen, carbon and hydrogen was performed to estimate the organic matter (OM) content using a Flash 2000 CHNS/O analyzer equipped with TCD detection system (Thermo Fisher, USA). The raw soil samples were heated to 1020 °C during 600 s and calculations were carried out employing EAGER XPERIENCE software (Thermo Fisher, USA). Prior to elemental analysis carbonates were eliminated by treating the raw soil with acetic acid (0.2 N) and washed with Milli-Q® water. For OM estimation, the C content of soil before and after hydrogen peroxide treatment (to remove any organic matter) was determined. To this end soil was dispersed in water (10 g/10 ml H_2O) and mixed with 50 ml of 20% H_2O_2 (wt/wt) solution at room T. The dispersion was stirred until frothing subsided. The treatment was repeated twice, and the sample was repeatedly washed with Milli-Q® water.

Field emission scanning electron microscopy (FESEM, AURIGA, Carl Zeiss, Germany) coupled with energy dispersive spectroscopy (EDS) microanalysis (INCA-200, Oxford, UK) was used to study the morphology and composition of carbon coated polished thin sections of fired bricks. The FESEM was operated at 10^{-6} Pa vacuum and 20 kV acceleration voltage for backscattered electron imaging and microanalysis. Additional SEM images and line scans were obtained using a Phenom XL scanning electron microscopy (Thermo Scientific, USA) coupled with EDS, working at 0.1 Pa vacuum and 15 kV acceleration voltage for backscattered electron imaging and microanalysis.

Skeletal density, porosity and pore size distribution of fired bricks (using two specimen per brick sample) were determined with mercury intrusion porosimetry (MIP) using an Autopore III 9410 porosimeter (Micromeritics, USA). This instrument measures pores with 0.003–360 μm diameter. Samples (~1 g) were dried at 110 °C for 3 h prior to analysis.

Parameters associated with fluid uptake and transport inside the bricks' pore system were determined by performing hydric tests in order to study water absorption [20] and drying behavior [21]. Tests were performed in triplicate under controlled laboratory conditions (20 ± 2 °C and 55 ± 5% RH) using Milli-Q® water. Parameters calculated from these tests are listed in Table 1:

To further evaluate the water absorption behavior, the sessile drop method was applied to determine the static contact angle of 4 μL water drops deposited on the bricks' surface using an OCA 15 EC equipment (DataPhysics Instruments, Germany) following the procedure described in UNE-EN 828 [24]. The same instrument was used to record videos of water drop absorption and determine changes in absorption kinetics of

Table 1
Calculated parameters and corresponding formulae and references.

Parameter	Formula	Reference
Skeletal density (ρ_{sk}, g cm^{-3})	$\rho_{sk} = \frac{M_0}{M_0 - M_h}$	[22]
Apparent density (ρ_a, g cm^{-3})	$\rho_a = \frac{M_0}{M_s - M_h}$	[22]
Open porosity (ϕ_o,%)	$\phi_t = \frac{M_s - M_0}{M_s - M_h} \times 100$	[22]
Free water absorption (A_b, %)	$A_b = \frac{M_l - M_0}{M_0} \times 100$	[20]
Forced water absorption (A_f, %)	$A_f = \frac{M_s - M_0}{M_0} \times 100$	[20]
Absorption coefficient (A_c)	$A_c = \frac{M_{4\min} - M_0}{M_0}$	[20]
Degree of pore interconnectivity (A_x, %)	$A_x = \frac{A_f - A_b}{A_f} \times 100$	[23]
Saturation coefficient (S)	$S = \frac{M_{48h} - M_0}{M_s - M_0}$	[22]
Drying index (DI)	$DI = \frac{\int_{t_0}^{t_f} f(M_t)dt}{M_s \times t_f}$	[21]

M_0 = dry sample mass, M_l = saturated sample mass at atm, $M_{4\,min}$ and $M_{48\,h}$ = saturated sample mass after 4 min and 48 h water absorption at atm, M_s = saturated sample mass under vacuum, M_h = hydrostatic sample weight saturated under vacuum, M_t = weight decrease of saturated sample over time.

bricks fired at different T. Average values are based on at least 3 measurements per brick type.

Compressive and flexural strength of fired bricks were determined with an Instron 3345 equipment (Instron Co., US) using an adapted version of the procedure described in EN 1015–11 [25]. Prismatic samples (4 ×1×1 cm for flexural strength, 3 samples per brick type) and (2 ×1×1 cm for compressive strength, 6 samples per brick type) were tested by applying a load of 5000 N at 3 mm/min.

To determine the elastic-dynamic properties of fired bricks a ultrasonic pulse velocity tester (58-E4800, Controls S.p.A., Italy) was used following ASTM D2845 [26]. Measurements of the propagation of P-waves in the three orthogonal directions (V_{P1}, V_{P2} and V_{P3}) were taken in triplicate using 54 kHz transducers (Ø = 27 mm) and water-based gel to ensure a homogeneous contact between the transducers and the brick surface. The anisotropy (ΔM) was calculated using the following equation: $\Delta M = [(V_{max}\text{-}V_{min})/V_{max}]$ x 100 (V_{max} and V_{min} being maximum and minimum velocities parallel and normal to the bedding plane, respectively).

The surface hardness (Leeb hardness, HLD) of fired bricks was measured using a durometer (rebound hammer, PCE-2500 N, PCE Instruments, Germany). Reported values are based on 10 measurements per specimen.

3. Results

3.1. Visual observations and color measurements of unfired and fired bricks

Color is an important parameter in the case of replacement bricks for heritage conservation interventions. The color of bricks is influenced by the mineralogical composition of the raw material, the firing T, and the kiln atmosphere [27], iron compounds being the main coloring agents leading to different shades of brownish-red colors under oxidizing conditions [28]. Color measurements (Table 2) are in good agreement with visual observations (Fig. 3 and Fig. S1, Supplementary Material), generally showing an increase in lightness in fired bricks as compared to the unfired bricks except for those fired at 1100 °C. This finding is in line with results by Rathossi and Pontikes [29], who also observed a lighter color of bricks upon firing. Bricks fired at 1100 °C experience the lowest color change (ΔE^*), which is, however, quite noticeable as it involves a decrease in b^*, leading to a more bluish color but does not alter lightness. In all other bricks, firing results in a shift towards more yellowish red colors, possibly due to the increase in hematite content (Fig. 3, see Section 3.2.) [28]. The addition of 1 wt% KOH leads to a significant increase in lightness and a color shift towards yellow in the unfired clay, which slightly reduces the overall color change induced by the firing process as compared to bricks without KOH.

Bricks fired at 1100 °C suffer swelling, manifested as a convex deformation of the cube`s faces and caused by the pressure built up of entrapped combustion gases due to the rapid formation of a dense vitrified outer layer. This vitrified layer hinders the diffusion of oxygen towards the core of bricks fired at 1100 °C. When split in half, they reveal a black inner core surrounded by a red rim, which suggests an oxygen-depleted environment caused by incomplete combustion of the soil`s organic matter [30], generating CO during firing (Fig. 3 and Fig. S1, Supplementary Material). The remaining bricks, with the exception of sample A800, show 3–4 mm thick outer rims of slightly darker color (Fig. 3), probably caused by an increased degree of vitrification [31]. Likely, the (partial) filling of surface pores by the newly formed glass phase upon vitrification is responsible for the darker color, as the refractive index of glass is higher (1.517) than that of air (1.003) and very close to that of common soil minerals [32], thus leading to a reduction in reflectance. However, the formation of this outer vitrified layer is slower in bricks fired at ≤ 950 °C and/or this layer is of lower density and does not hinder the access of oxygen to the core (i.e., the formation of a black core is not observed). Finally, bricks containing KOH (samples AK800 and especially AK950, Fig. 3) show limited formation of up to 800 μm wide cracks upon firing.

Table 2
Color parameters of the outer surface of bricks fired at different T, standard deviation being included.

Sample	L^*	a^*	b^*	ΔL^*	Δa^*	Δb^*	ΔE^*
A unfired	40.75 ±0.50	18.20 ±0.35	21.97 ±0.49				
A 800 °C	47.96 ±2.10	26.87 ±0.74	29.80 ±1.32	7.21 ±2.10	8.67 ±0.74	7.82 ±1.32	13.82 ±1.93
A 950 °C	47.04 ±2.76	25.71 ±1.16	26.88 ±2.39	6.29 ±2.76	7.51 ±1.16	4.91 ±2.39	11.13 ±3.18
A 1100 °C	41.00 ±1.40	19.78 2.83	18.04 ±3.16	0.61 ±1.22	2.39 ±2.25	-3.12 ±2.74	5.16 ±0.72
AK unfired	46.28 ±1.30	19.41 ±0.18	25.73 0.89				
AK 800 °C	49.79 ±2.98	26.57 ±1.33	30.32 ±1.31	3.52 ±2.98	7.16 ±1.33	4.59 ±1.31	9.69 ±0.99
AK 950 °C	51.34 ±1.53	26.69 ±0.90	29.65 ±1.39	5.07 ±1.53	7.28 ±0.90	3.92 ±1.39	9.85 ±1.20

L^* = lightness, varying from black with a value of 0 to white with a value of 100; a^* and b^* = chromaticity coordinates, a^* varies from $+a^*$ (red) to $-a^*$ (green) and b^* from $+b^*$(yellow) to $-b^*$ (blue); and ΔE^* = color change.

3.2. Mineralogical evolution upon firing

According to XRD analysis using the Rietveld method, the raw soil mainly contains quartz (~55 wt%) and phyllosilicates (25–30 wt%) along with small amounts (~5 wt%) of feldspars (orthoclase), carbonates (calcite/dolomite), and traces of hematite (Table 3), the latter being responsible for the intense red color of the raw soil. The clay fraction is primarily comprised of illite/muscovite (~15 wt%) and paragonite (≤10 wt%), together with minor amounts of kaolinite, smectites and interstratified illite/smectite. Note that no attempt has been made to quantify the latter two phases as their low crystallinity does not allow a reliable quantification and they are thus not included in Table 3. Chemical analysis results (Table 4) are compatible with the mineralogical composition, confirming a significant content in iron associated with oxihydroxides and, to a certain extent, clay minerals. The relatively high iron content determined by XRF suggests that a portion of the iron-rich minerals in the raw soil is amorphous, since only a very limited amount of crystalline hematite (~1 wt%) is detected, while the amorphous phase content is ~9 wt% according to Rietveld analysis (Table 3). Based on the relatively small amounts of calcite and dolomite the soil can be classified as carbonate-poor [33].

Firing at 800 °C results in a partial decomposition of carbonates and the dehydroxylation of clay minerals, and only reduced amounts of dehydroxylated muscovite and paragonite are detectable while kaolinite is no longer present (Table 3). Generally, alkali feldspars act as flux and are consumed upon crystallization of high-T phases [34]. However, here decomposition of clay minerals seems to have resulted in a slight increase in orthoclase at 800 °C, while new high-T phases are not observed. At 950 °C, carbonates are no longer detected and the muscovite and paragonite content decreases. The hematite content continuously increases with firing T. In a clayey material, several reactions might be responsible for this increase, including decomposition of Fe-rich phyllosilicates, dehydroxylation of goethite (not detected with XRD) and crystallization of previously amorphous oxihydroxides [28,35]. According to Nodari et al. [30], hematite formation may occur at temperatures as low as 800 °C, depending on soaking time. At 1100 °C, hematite experiences a further increase and hercynite ($FeAl_2O_4$), which quite commonly forms under reducing conditions, is also observed [36,37]. According to XRD analysis, the concentration of hercynite is higher in the black core of the fired brick (sample A1100B), which is consistent with its black color. The presence of carbon (graphite) and wüstite, which are commonly associated with the black color [38], could not be

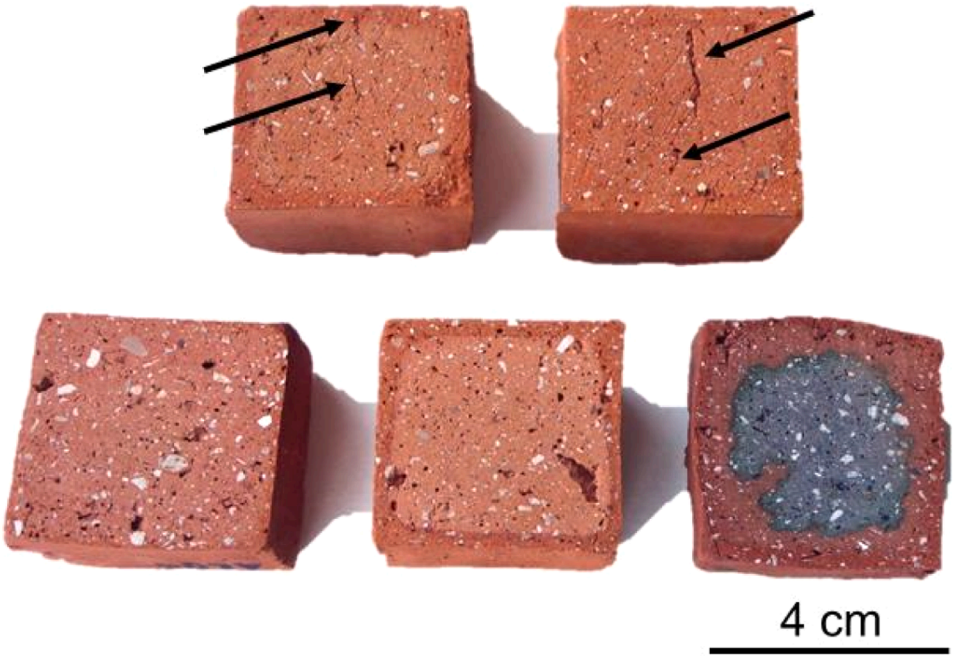

Fig. 3. Photographic images of bricks split in half, fired at different *T*. Bricks with 1 wt% KOH (upper row, some firing cracks can be observed, black arrows) and without KOH (lower row).

Table 3
Mineralogical composition (wt%) according to XRD (Rietveld) analysis.

Mineral	A0	A800	A950	A1100R	A1100B	AK0	AK800	AK950
Quartz	55.2	55.7	58.6	62.9	58.1	55.9	57.7	59.4
Calcite	2.9	3.6	-	-	-	3.5	2.8	-
Dolomite	2.1	-	-	-	-	1.9	0.3	-
Kaolinite	3.4	-	-	-	-	3.2	-	-
Muscovite	15.4	13.0	5.3	-	-	15.1	11.3	2.8
Paragonite	8.0	5.6	3.3	-	-	8.0	3.0	0.9
Hematite	1.1	2.0	2.8	2.4	3.2	1.1	1.6	3.0
Orthoclase	3.0	4.7	4.0	-	-	2.2	4.8	4.2
Anorthite	-	-	-	5.6	6.2	-	-	-
Mullite	-	-	-	5.0	4.2	-	-	-
Hercynite	-	-	-	1.9	3.9	-	-	-
Amorph.	8.8	15.5	26.1	22.2	24.5	9.1	18.6	28.8

Table 4
Chemical analysis of major elements (wt%) of raw soil based on XRF analysis.

Sample	SiO_2	Al_2O_3	Fe_2O_3	MgO	CaO	Na_2O	K_2O	TiO_2	LOI*
Soil	63.68	16.14	7.33	0.94	1.70	0.55	1.72	0.61	7.24

* LOI = loss on ignition

confirmed with XRD. The limited amount of hercynite in the rim (sample A1100R) resulted in a bluish red color in contrast to the yellowish red color of bricks fired at lower *T* (Fig. 3). Other high-*T* phases such as mullite ($Al_{(4+2x)}Si_{(2-2x)}O_{(10-x)}$) and anorthite (see section X) are also detected at 1100 °C, which are commonly formed upon muscovite decomposition where H_2O and K play a key role as melting agent [39]. The quartz content increases slightly as firing *T* was raised. The amorphous content also shows a positive correlation with firing *T*, being slightly higher in bricks with KOH (Table 3), which is to be expected as this compound acts as flux and lowers the melting temperature of the silicate minerals [15]. Remarkably, the amorphous phase content of the black zone associated with an oxygen-depleted environment is slightly higher than that of the red zone of bricks fired at 1100 °C, suggesting a higher degree of vitrification in the former. This result is in line with findings by Rathossi and Pontikes [29], who found that the formation of melting phases is favored under reducing conditions in clays with low carbonate content.

Differences in the oxidation state of iron in the black and red zones of bricks fired at 1100 °C are further studied using XPS (Fig. 4). Deconvolution of the Fe 3p band reveals the presence of two components centered at 54.7 and 57.4 eV, which are assigned to Fe^{2+} and Fe^{3+}, respectively [40]. The black zone has a higher Fe^{2+}/Fe^{3+} ratio (i.e., 1.4) as compared to the red zone (i.e., 1.0), which is likely related with the larger amount of hercynite. This finding is in agreement with XRD results and confirms the reducing firing conditions in the brick core (i.e., black zone). However, it cannot be ruled out that a small portion of Fe^{2+} is also linked to the presence of mullite, which is detected in both zones. According to Schneider and Rager [41], iron occurs predominately as Fe^{3+} in mullite and only minor amounts of Fe^{2+} enter in mullite under strong reducing conditions. A large portion of Fe^{3+} is certainly

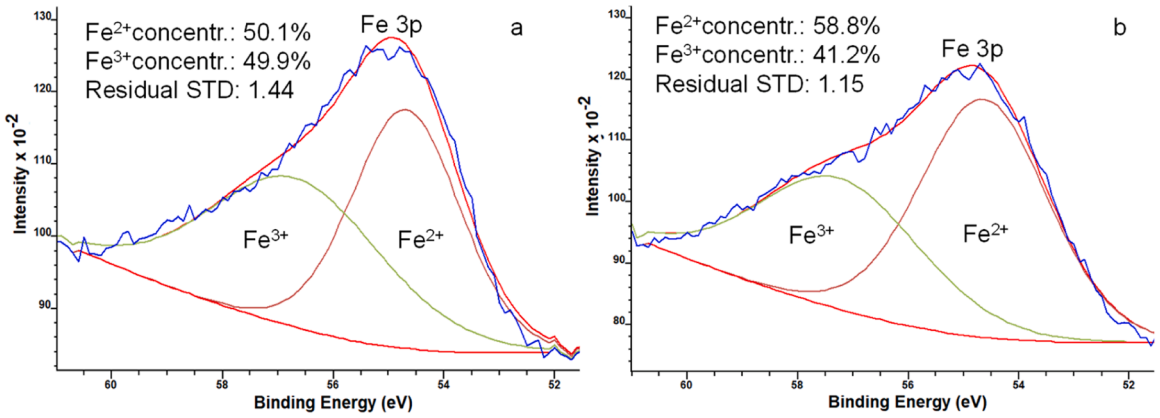

Fig. 4. XPS spectra of the Fe 3p band of the red (a) and black (b) areas of a brick fired at 1100 °C. Deconvolution revealed a higher Fe^{2+}/Fe^{3+} ratio in the black area as compared to the red area.

associated with the presence of hematite, which is detected in black and red zones with XRD.

SEM imaging and microanalysis give additional information on transformation reactions upon brick firing (Fig. 5). Phase changes and final elemental compositions of reaction products show local variations and a clear correlation with the composition of adjacent mineral grains. In the case of a K/Na-rich feldspar grain in direct proximity to a dolomite grain, significant enrichment in Ca upon firing at 950 °C is detected (Fig. 5a). The Ca concentration gradually decreases towards the core of the feldspar grain, being accompanied by a concomitant increase in K and Na. At the interface between carbonate and feldspar, a ~1.5 μm thick reaction rim composed of a new calcium/magnesium-rich aluminosilicate phase is detected (Fig. 5a, arrow).

Dolomite grains suffer de-mixing upon firing (Fig. 5b). The EDS line profile of a decomposed dolomite grain in a brick fired at 1100 °C evidences the low mobility of Mg. Mg is concentrated in the core of the grain, while calcium diffuses out (Ca content of the core being <1 at%) and forms a reaction rim rich in Ca, Si, and Al. The Mg concentration of this rim is significantly lower than that of the core and decreases towards the outer border. Between the core and the reaction rim a 4–7 μm wide gap has formed that can be explained by the volume decrease upon thermal decomposition of dolomite, which led to a contraction and the formation of a porous core (Fig. 5b, inset), presumably an iron-rich periclase. These changes seem reasonable, considering the volume reduction upon decomposition of dolomite. Indeed, the decomposition of $CaMg(CO_3)_2$ to MgO will lead to a ~80% volume reduction, based on

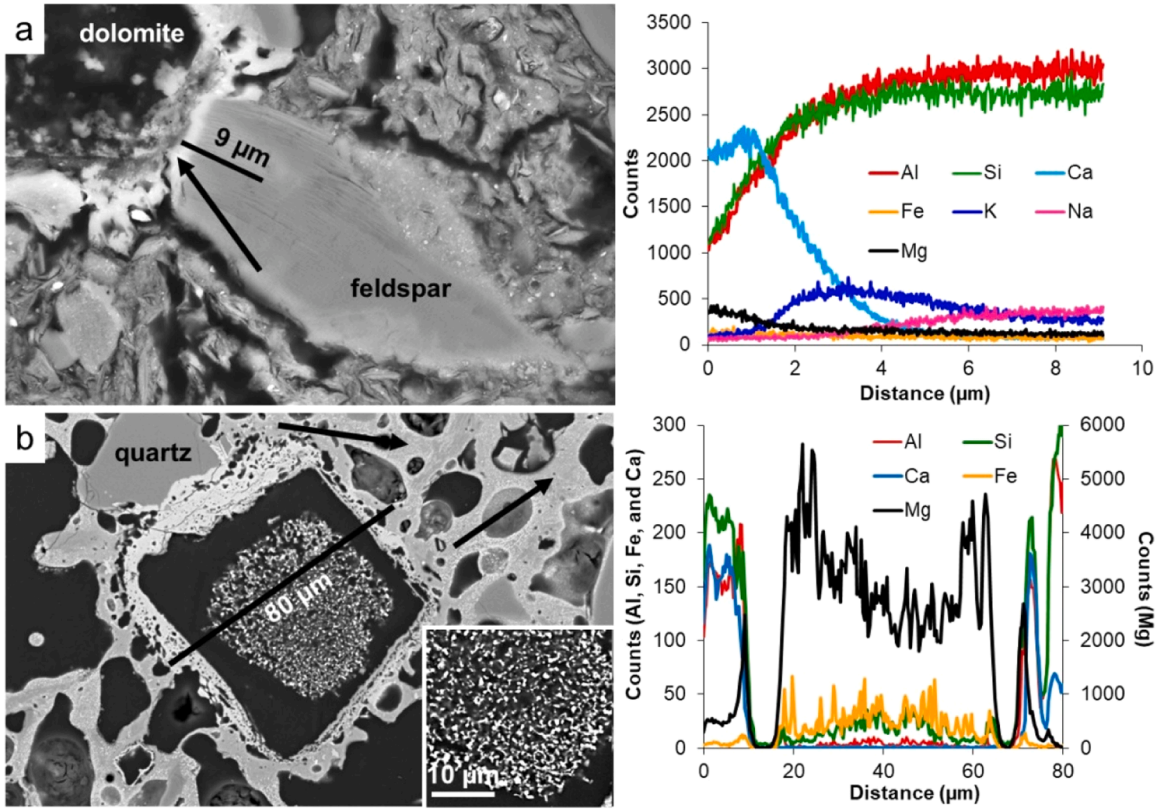

Fig. 5. SEM backscattered electron images and corresponding EDS line profiles (black lines indicate the location of the analyses) of: (a) feldspar grain in a brick fired at 950 °C (sample AK950, arrow indicates newly formed Ca/Mg-rich aluminosilicate phase), and (b) decomposed dolomite grain surrounded by a Ca-rich reaction rim in the black zone of a brick fired at 1100 °C (sample A1100B, detail of the former carbonate grain in inset, arrows indicate matrix).

the molar volumes of $CaCO_3$ (36.92 cm^3/mol), $MgCO_3$ (28.50 cm^3/mol), and MgO (11.26 cm3/mol). The Mg-rich cores seem to act as a sink for Fe in the brick sample fired at 1100 °C, its concentration being significantly higher in the core as compared to the adjacent Ca-rich reaction rim (Table 5). This behavior is only observed in the black zone, revealing a 7 times higher iron content as compared to Mg-rich cores in the red zone. The iron distribution in the matrix of red and black zones of bricks fired at 1100 °C also differs and is almost 30% higher in the red zone as compared to the black zone.

3.3. Organic matter (OM) content of the soil

According to elemental analysis, the untreated soil sample and the sample treated with H_2O_2 to remove any organic matter, contain 1.18 and 0.20 wt% total carbon (C), respectively. The 0.20 wt% carbon in the H_2O_2-treated soil sample presumably corresponds to black carbon (i.e., graphitic and pre-graphitic phases such as charcoal, graphite, soot and coal), which withstands strong chemical or thermal oxidation and is considered inert [42]. The difference in total carbon content between the untreated soil sample and the sample treated with H_2O_2 corresponds to organic carbon and is used to calculate the OM content based on the assumption that OM in soils is constituted of ~58% organic carbon [43]. Thus, the calculated OM content of the untreated soil amounts to 1.7 wt %. However, it cannot be ruled out that the OM content is slightly underestimated as the H_2O_2 treatment might has removed only about 87% of the initial organic carbon [42].

3.4. Density and porosity of fired bricks

Skeletal density values (2.61–2.78 g cm^{-3}) based on MIP measurements (Table 6) are coherent with those reported for the bricks` main mineral constituents including quartz (2.62 g cm^{-3}), clays (2.40–2.80 g cm^{-3}), feldspars (~2.70 g cm^{-3}), and carbonates (2.70–2.85 g cm^{-3}). Skeletal densities calculated from water absorption data of samples A950 (2.38 g cm^{-3}) and A1100 (2.14 g cm^{-3}) are significantly lower than ρ_{MIP}, which suggests that part of the pores in these bricks are inaccessible to water, even under vacuum. These discrepancies can be explained by the fact that only a small brick fragment was used for MIP, while the entire brick was subjected to the water absorption test, where the vitrified outer layer obstructed the access to part of the pores. This effect is not observed in samples fired at 800 °C with a lower degree of vitrification. In the case of the sample containing KOH and fired at 950 °C, the "sealing" effect of the vitrified outer layer seems to be cancelled out by crack formation. Consequently, the skeletal densities ρ_{MIP} and ρ_{sk} of these samples do not show important differences and are in good agreement with previously reported values for bricks made with low-carbonate clays [44].

Porosity (Table 6) calculated from water absorption data (ϕ_o) shows a negative relation with firing T and is ~20–30% higher in bricks with KOH as compared to their KOH-free counterparts which could, at least in part, be related to the observed crack formation in the former. MIP porosity (ϕ_{MIP}) values are in good agreement with porosity values calculated based on water absorption data in the case of bricks containing KOH, but are 10–15% higher than ϕ_o values of KOH-free bricks fired at 800–950 °C. The difference is even higher (30–80%) in the case of KOH-free bricks fired at 1100 °C. Remarkably, firing at 1100 °C does not further decrease porosity and values are almost 40% higher in the black zones as compared to the red zones likely due to the expansion of entrapped gases (see below).

MIP reveals some clear trends regarding the pore size distribution (Table 6). All bricks fired ≤ 950 °C show a similar volume (~10%) of pores > 10 μm diameter. With the increase in firing T from 800 to 950 °C, the volume corresponding to pores with a diameter > 1 μm increases by ~10–15%, while the volume of pores < 0.1 μm decreases by ~10%, pore size evolution being similar in bricks with and without KOH. In samples fired at 1100 °C, increased vitrification results in a further decrease in pores with a diameter < 0.1 μm, which amounted to only ~5% of the total pore volume. Remarkably, MIP results indicate a significant difference in the volume corresponding to pores with a diameter > 1 μm between the red (70%) and black (32%) areas of bricks fired at 1100 °C. Comparison with SEM images reveals that MIP is not able to correctly describe the pore size distribution of these samples (Fig. 6). Apparently, the ink bottle effect [45] leads to a dramatic underestimation of large pores (≥30 μm), which is especially significant in the case of the sample corresponding to the black zone, being dominated by fewer but extremely large pores (up to 50 μm in size). These pores likely form upon coalescence of smaller pores [23] and/or are the result of the entrapped gases which expand during firing. The formation of

Table 5
Chemical composition (at%) of decomposed carbonate grains, reaction rims, and brick matrix of the black and red zones in bricks fired at 1100 °C based on SEM-EDS point analysis (minimum 10 analyses, standard deviation being included).

	Carbonate grain		Reaction rim		Matrix	
Element	Black	Red	Black	Red	Black	Red
Oxygen	48.1 ± 1.8	44.3 ± 5.7	53.6 ± 2.7	52.1 ± 2.2	61.9 ± 0.3	61.8 ± 0.2
Aluminum	0.7 ± 0.8	0.6 ± 0.7	13.4 ± 1.8	13.7 ± 2.0	17.9 ± 0.5	17.5 ± 0.4
Silicon	1.3 ± 1.0	2.5 ± 1.2	11.7 ± 0.8	12.5 ± 1.5	13.9 ± 0.5	13.9 ± 0.4
Calcium	0.2 ± 0.3	0.4 ± 0.5	16.5 ± 1.9	17.5 ± 3.5	0.4 ± 0.2	0.4 ± 0.2
Iron	6.4 ± 0.8	0.9 ± 0.7	1.0 ± 0.7	1.8 ± 0.7	2.4 ± 0.6	3.3 ± 0.5
Magnesium	43.2 ± 1.4	51.3 ± 5.7	3.6 ± 1.6	2.5 ± 1.0	0.9 ± 0.3	0.9 ± 0.2
Potassium	0.0 ± 0.0	0.0 ± 0.0	0.0 ± 0.0	0.0 ± 0.0	1.7 ± 0.2	1.5 ± 0.1

Table 6
Physical parameters of bricks fired at different T, standard deviation being included.

Sample	A800	A950	A1100	AK800	AK950
ρ_{sk}	2.53 ± 0.07	2.38 ± 0.03	2.14 ± 0.06	2.65 ± 0.01	2.60 ± 0.01
ρ_a	1.76 ± 0.00	1.75 ± 0.01	1.63 ± 0.06	1.68 ± 0.01	1.70 ± 0.01
ρ_{MIP}	2.78 ± 0.02	2.61 ± 0.18	(red) 2.64 ± 0.07 (back) 2.77 ± 0.06	2.77 ± 0.11	2.68 ± 0.06
ϕ_o	30.47 ± 1.81	26.56 ± 1.12	23.90 ± 1.04	36.66 ± 0.27	34.67 ± 0.63
ϕ_{MIP}	33.97 ± 3.08	30.31 ± 0.28	(red) 30.83 ± 1.78 (black) 42.73 ± 2.38	37.59 ± 0.47	34.98 ± 1.41
Pore Ø > 10 μm	12.5 ± 1.7	12.2 ± 3.2	(red) 19.1 ± 4.8 (black) 12.2 ± 3.6	12.8 ± 0.8	10.2 ± 4.0
Pore Ø > 3 μm	18.0 ± 0.3	18.8 ± 0.3	(red) 48.0 ± 13.8 (black) 17.9 ± 6.0	19.7 ± 4.8	19.0 ± 0.6
Pore Ø > 1 μm	37.1 ± 4.5	49.4 ± 2.3	(red) 69.5 ± 19.5 (black) 31.9 ± 12.9	40.1 ± 7.5	54.2 ± 11.6
Pore Ø < 0.1 μm	26.8 ± 5.8	17.6 ± 0.4	(red) 5.2 ± 4.8 (black) 3.9 ± 1.8	28.2 ± 10.2	13.7 ± 11.1

Skeletal density (ρ_{sk}, g cm^{-3}); apparent density (ρ_a, g cm^{-3}); MIP density (ρ_{MIP}, g cm^{-3}); open porosity (ϕ_o, %); MIP porosity (ϕ_{MIP}, %), and pore size distribution (volume of pores with different Ø, %), standard deviation included.

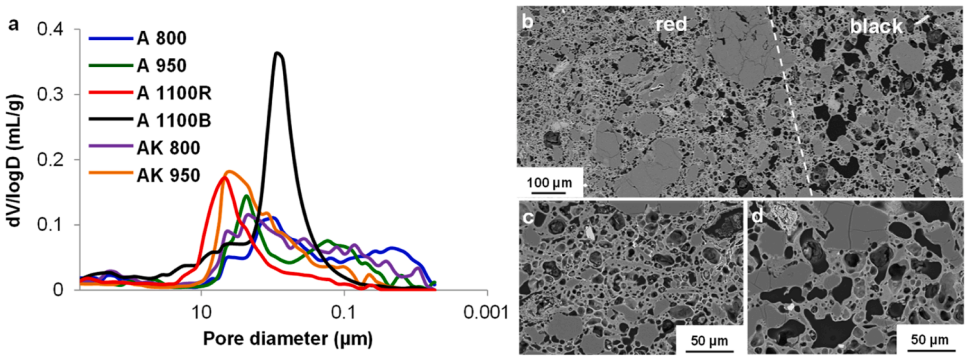

Fig. 6. Pore size distribution of fired bricks. (a) Pore size distribution based on MIP and (b) SEM backscattered electron images of the brick fired at 1100 °C, revealing significant difference between the pore size distribution of the red outer zone (c) and the black core (d), the latter showing a large number of pores ≥ 30 µm. According to MIP the porosity was ~30% higher in the black core (~43%) than the red outer zone (~31%).

large rounded pores is probably facilitated by a more viscose melt and advanced degree of vitrification under oxygen-depleted conditions (Fig. 6b) as evidenced by the higher amorphous content according to XRD-Rietveld results (Table 3).

3.5. Hydric behavior

The free and forced water absorption capacity shows a negative correlation with firing temperature and is 26–39% higher in bricks containing KOH as compared to their KOH-free counterparts (Table 7, Fig. 7), being in line with the higher porosity of the former (Table 6). The water absorption capacity is linked to durability, higher values being indicative of lower durability. Thus, KOH-free should be preferable, even though, all bricks comply with ASTM requirements for either severe (water absorption ≤0.20) or moderate weathering-grade bricks (water absorption ≤0.25) [46]. Remarkably, the absorption coefficient (A_c) is substantially higher for bricks containing KOH. This is probably related to crack formation during firing [23], which is much more pronounced in bricks containing KOH and results in faster absorption immediately upon contact with water. The difference in free and forced water absorption is greatest in bricks fired at 1100 °C and smallest in the ones containing KOH fired at 800 °C. Consequently, these were the bricks showing the lowest and highest pore interconnectivity (highest and lowest A_x value), respectively. Overall, A_x values show a positive correlation with firing temperature, which can be explained by the gradual increase in vitrification (Table 3), rendering the pore network more tortuous and less accessible (Table 7). However, the effect of increased vitrification seems to be counterbalanced by crack formation in the case of bricks containing KOH, which reveal systematically lower A_x values as compared to their KOH-free counterparts. The saturation coefficient (S) is clearly linked and inversely related to pore interconnectivity (A_x), bricks with a better communicated pore network reaching higher saturation because water is able to enter in most pores under ambient conditions without the need to apply a vacuum in order to force absorption. The saturation coefficient decreases markedly at higher firing temperatures in the case of KOH-free bricks, while the decrease is only minor in bricks containing KOH, likely being due to the presence of cracks. According to the RILEM commission 25-PEM (1980 [22]), bricks with high saturation (S) coefficients might be more prone to deterioration. However, all bricks comply with ASTM requirements for severe (saturation index ≤ 0.80) or moderate weathering-grade bricks (saturation index ≤ 0.90) [48]. The drying index is similar for all bricks (Table 7) and some overlapping of curves is observed during the falling drying rate period. However, drying during the first 48 h (Fig. 7) seems to be slower in the case of KOH-free bricks fired at ≥ 950 °C ($y \approx 0.0027x$) as compared to the remaining bricks ($y \approx 0.0038x$), likely due to a more tortuous pore network (higher A_x values) and the presence of difficult to access pores (indicated by the lower skeletal porosity) that delayed or hindered water transport.

Table 7
Hydric parameters and contact angle of bricks fired at different T, standard deviation being included.

Sample	A800	A950	A1100	AK800	AK950
A_b	15.77 ± 1.19	13.66 ± 0.71	12.20 ± 0.10	20.72 ± 0.97	18.94 ± 0.54
A_f	17.31 ± 1.01	15.18 ± 0.68	14.68 ± 1.11	21.86 ± 0.61	20.42 ± 0.52
A_c	0.07 ± 0.00	0.07 ± 0.01	0.05 ± 0.00	0.12 ± 0.00	0.13 ± 0.00
A_x	8.99 ± 1.60	10.00 ± 0.63	16.61 ± 5.62	5.24 ± 1.08	7.25 ± 0.57
S	0.77 ± 0.02	0.72 ± 0.01	0.60 ± 0.04	0.81 ± 0.01	0.77 ± 0.01
DI	0.90 ± 0.00	0.90 ± 0.00	0.90 ± 0.00	0.89 ± 0.00	0.89 ± 0.00
θ	77.8 ± 2.8	92.6 ± 3.7	88.5 ± 8.3	77.2 ± 4.0	90.3 ± 1.4
W	25.3 ± 3.7	21.4 ± 4.9	53.2 ± 7.4	18.9 ± 5.3	48.7 ± 8.1

Free water absorption (A_b, %); forced water absorption (A_f, %); absorption coefficient (A_c); degree of pore interconnectivity (A_x, %); saturation coefficient (S); drying index (DI); contact angle (θ, °); and water drop absorption (W, s).

Contact angle measurements (Table 7) give further insight into the hydric behavior of fired bricks. The wettability state of all bricks falls into the intermediate-wet range according to the classification by Iglauer et al. [47], even though water drop absorption took twice as long in the case of bricks containing KOH and fired at 950 °C and KOH-free bricks fired at 1100 °C as compared to the remaining bricks. The relative fast water drop absorption in the case of the KOH-free brick fired at 950 °C is puzzling as it is not consistent with the measured contact angle. This discrepancy requires further investigation as it is not caused by an experimental error (i.e., the reported value is based on 8 measurements). Generally, contact angle values increase when the firing temperature is raised from 800 to 950 °C independent of KOH content but do not show any further increase at 1100 °C. The surfaces of all bricks fired ≥ 950 °C show contact angles ~90° and can be, thus, considered hydrophobic, while those of bricks fired at 800 °C are slightly hydrophilic with contact angles ~77°.

3.6. Mechanical properties

Flexural and compressive strength as well as surface hardness all show a positive relation with firing temperature (Fig. 8, Table S2, Supplementary Material). The effect of KOH on strength is inconclusive (i.e., KOH addition leading to slightly higher flexural but lower compressive strength as compared to KOH-free counterparts) and requires further research to determine in how far the positive effect of the slightly higher vitrification degree (Table 3) is offset by the higher porosity (Table 6) and propensity for crack formation (Fig. 3). While

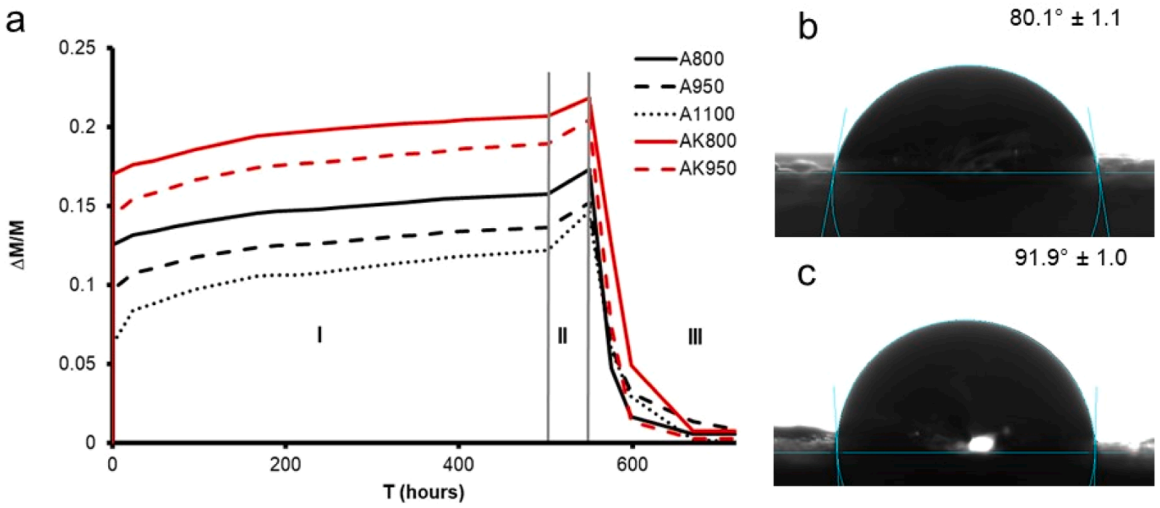

Fig. 7. (a) Weight change due to free (I) and forced (II) water absorption and drying (III) of bricks fired at different *T*, (b) and (c) representative contact angle measurements of samples AK800 and AK950, respectively.

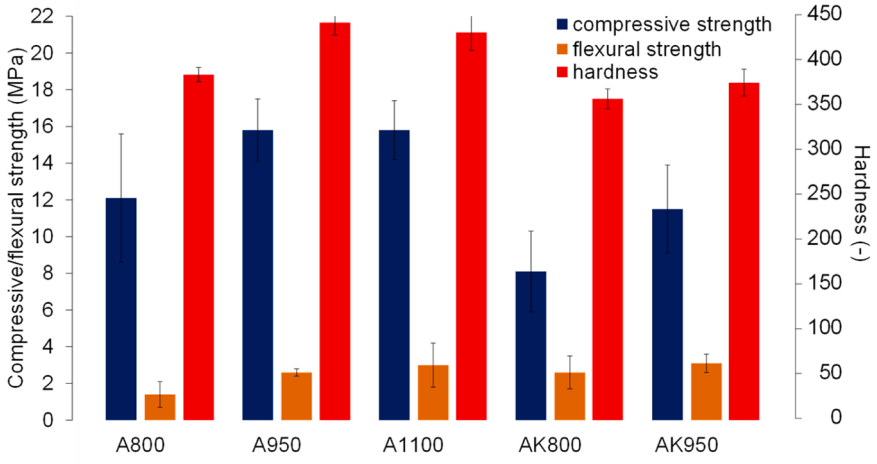

Fig. 8. Mechanical properties of bricks fired at different *T*, error bars indicating standard deviation.

extensive compressive strength data for bricks has been published, information regarding flexural strength is limited. Reported flexural strength values for old (4.3–5.2 MPa [48]) and new bricks fired at comparable temperatures (3.5–6.5 MPa [48,49]) are somewhat higher than those of this study (1.4–3.1 MPa). However, it has to be considered that brick samples of reduced size were used for testing here and small imperfections due to the manual fabrication have probably affected measurements as the considerable data spread suggests.

All bricks, except the ones containing KOH and fired at 800 °C, fulfill the compressive strength requirement (9.8 MPa) according to the Spanish building code [50]. High compressive strength is associated with improved durability [51]. Indeed, the American building code relates compressive strength requirements to different grades of weathering resistance. All bricks of this study fulfill the requirement for negligible weathering-grade bricks (8.6 MPa) and KOH-free bricks fired at ≥950 °C even comply with that for moderate weathering-grade bricks (15.2 MPa [46]). No difference in compressive strength between KOH-free bricks fired at 950 and 1100 °C is observed. This contradicts previous findings [8] but seems reasonable as neither an increase in vitrification (according to XRD-Rietveld analysis) nor a reduction in porosity are detected in bricks fired at 1100 °C as compared to their counterparts fired at 950 °C. Remarkably, bricks fired at ≤950 °C containing KOH reveal greater plastic deformability (strain = 0.14 ± 0.01) as compared to their KOH-free counterparts (strain = 0.09 ± 0.01), which could be advantageous in order to limit damage created by movement due to foundation settlement or seismic activity.

Surface hardness (Fig. 8, Table S2, Supplementary Material) shows a positive relation with firing temperature, KOH-free bricks revealing systematically higher hardness as compared to bricks containing KOH. These results are in line with the higher compressive strength detected in KOH-free bricks and seem to be related to porosity, bricks with lower porosity showing higher surface hardness and compressive strength (Table 6).

Ultrasound velocity measurements give additional information on the compactness of fired bricks (Table 8). Not surprisingly, the lowest velocity is always measured normal to bedding and it increases as the

Table 8
Ultrasound velocity measurements (m s^{-1}) and anisotropy (ΔM) of bricks fired at different *T*, standard deviation being included.

Sample	V_{P1}	V_{P2}	V_{P3}	ΔM
A800	1446 ± 157	1699 ± 153	1825 ± 123	20.9 ± 4.2
A950	1908 ± 43	1985 ± 51	2159 ± 59	11.6 ± 1.6
A1100	2027 ± 87	2105 ± 85	2183 ± 38	7.1 ± 4.0
AK800	1158 ± 92	1506 ± 119	1578 ± 105	26.65 ± 1.4
AK950	1479 ± 69	1802 ± 85	1876 ± 118	21.02 ± 5.0

firing T is raised. Firing at 1100 °C does not further improve compactness and differences in velocity compared to bricks fired at 950 °C are all within error. This is in line with reported porosity (Table 6) and strength data (Fig. 8). Anisotropy shows a negative correlation with firing T due to the decomposition of sheet minerals, giving way to high temperature phases, which no longer show a laminar morphology, as well as the formation of more rounded voids without any preferred orientation especially in the case of bricks fired at 1100 °C (Fig. 6) [52,53]. The addition of KOH leads to a systematic decrease in velocity, which was more pronounced normal to bedding (20–22%) as compared to the directions parallel to bedding (9–14%), and is likely related to higher porosity and possibly crack formation detected in bricks containing KOH. The data of this study is in fairly good agreement with velocity values (1075–2483 m s^{-1}) reported by Justicia Muñoz et al. [10] for historic bricks from the Colegio Máximo de Cartuja in Granada (Spain), which were likely fabricated with soil from the same outcrop (Alhambra formation) as those analyzed in this study. Reported anisotropy values ($\Delta M = 17.4 - 36.6$ [10]) span over a wide range, and extremely high values are likely related to low firing temperatures (i.e., presence of phyllosilicate sheets and matrix with low vitrification degree) and/or deterioration processes undergone by the historic bricks.

4. Discussion

Findings of this study prove that Alhambra Formation soil is suitable for the fabrication of replacement bricks, even though the firing process would have to be optimized in order to allow for $T > 950$ °C without the risk of deformation. A lower heating rate could be employed to delay the formation of an impermeable outer vitrification layer and allow for sufficient oxygen diffusion into the core to facilitate complete combustion of organics and the release of combustion gases to prevent pressure built up [40]. Besides, it is revealed that a relatively low organic matter content (i.e., 1.7 wt%) is sufficient to create the black core in the case of bricks fired at 1100 °C, which is associated with reducing conditions [54].

A comparison of the red and black zone of bricks fired at 1100 °C gives important clues regarding the influence of the oxidation state of iron on the textural properties of the fired bricks. Various researchers have observed a negative correlation of Fe^{2+} content and melt viscosity that could explain the textural differences between red and black zones of bricks fired at 1100 °C in this study (Fig. 6) [55,56]. Mysen et al. [57] highlight the relation between redox equilibria and melt structure. According to these authors, ferrous iron (likely in octahedral coordination) only acts as network modifier, while ferric iron can either be a modifier or network former, depending on its coordination (tetrahedral or octahedral coordination). The coordination in turn is influenced by the ratio $Fe^{3+}/\Sigma Fe$ and ultimately the availability of charge-balancing alkali (earth) metal cations, a higher Fe^{3+} content favoring melt polymerization and leading to higher melt viscosity. The latter might explain the detected differences in the development of the porous system depending on redox conditions, showing a network of relatively large, spherical, and predominantly closed pores and a higher amorphous content in a reducing atmosphere (Fig. 5 and Table 3) [29].

The data obtained in this study suggest that replacement bricks for heritage conservation with matching porosity can be fabricated in the majority of cases, especially considering that common compatibility criteria stipulate that replacement materials should have higher porosity and larger pores in order to act as a sacrificial substrate (e.g., facilitating salt crystallization [58]). Indeed, porosity data for historic bricks (Table S1) show important variations, reported MIP porosity values of bricks from the Alhambra fortress and various historic buildings in Toledo (Spain), Cahors (France), and Mosul (Iraq) ranging from 22 - 44% [4,59–61]. In some cases, dissolution-precipitation reactions likely cause changes in the original pore system and either reduce the value due to salt precipitation or increase it due to weathering processes (i.e., water erosion, salt or freeze-thaw weathering or thermal expansion). Pore size distribution also determines weathering resistance. According to Maage [62] and Koroth et al. [51] a low proportion of pores with a diameter < 3 μm contribute to better durability. Bricks in this study fired at ≤ 950 °C (Table 6) do not show important variation in the volume of pores > 3 μm in size upon firing and are not frost resistant according to the durability index (DIM) established by Maage ($DIM = (3.2/\ \phi_{MIP}) + (2.4 * \phi$ pores > 3 μm [62]), having DIM values of ~45 (i.e., according to Maage [62], bricks with DIM <55 are not frost resistant). Samples corresponding to the red zone of bricks fired at 1100 °C, in contrast, show DIM values > 68.5 and are thus more frost resistant. Note that DIM cannot be calculated for the black areas of bricks fired at 1100 °C as it is impossible to correctly determine the volume of pores with a diameter > 3 μm due to the ink-bottle effect. However, SEM imaging shows that pores with a diameter > 3 μm are very abundant in the black core (more abundant than in the red rim), which suggests that these cores likely have DIM values higher than those of the red rims.

The opposite effect of KOH on flexural and compressive strength is probably related to the fact that KOH, being a strong electrolyte, induces flocculation of clay minerals in the wet green body [63]. Flocculation negatively affects bonding between the individual clay aggregates and leads to increased porosity in the fired body as evidenced by MIP measurements. Flocculation is probably also responsible for the formation of microcracks during drying, which widen upon firing (Fig. 3). Reduced bonding between clay aggregates does not seem to be offset by the slightly higher degree of vitrification upon firing as compared to the KOH-free bricks (Table 3). As a result, bricks containing KOH show greater plastic deformability, resulting in lower compressive strength. However, the more plastic behavior of bricks containing KOH leads to an increase in toughness and makes the material more tolerant to physical-mechanical stress during bending tests.

Matching the mechanical characteristics of historic bricks is a basic requirement of replacement bricks [61,64]. Reported compressive strength values vary significantly, spanning over a range of 6.7–28.0 MPa for bricks from historic buildings in Portugal, Poland, Spain and Australia, respectively [48,65–67]. Very low compressive strength values are likely related to advanced deterioration [66], underscoring the need for replacement bricks as some of the reported values fall below the minimum requirements of international building codes, thus suggesting possible safety problems with regards to the building's structural integrity [46,51]. Considering the relatively wide range of compressive strength data, it seems possible to fabricate bricks with adequate strength in most cases, taking into account common compatibility requirements that demand similar strength (e.g., according to specifications for building stone by Graue et al. [68], the replacement material should have 80–120% of the strength of the original material).

Detailed SEM analyses provide some interesting results regarding the mineralogical evolution upon firing, proving that at least part of the calcium-rich feldspar (anorthite) forms via solid state reaction through diffusion of Ca into the feldspar and does not necessarily involve crystallization after a melting process at the expense of clay minerals, quartz and calcite [69,70]. Ballato et al. [71] have suggested that anorthite would form via solid state reaction based on full-profile fitting analysis using the Rietveld method but did not provide direct evidence. Here, counterdiffusion of Si and Al led to the formation of a reaction rim composed of a new calcium/magnesium-rich aluminosilicate phase (Fig. 5a, arrow). In contrast to Ca, an increased Mg content is only detected in the reaction rim (i.e. Mg concentration of the rim being 1.6 at%), but not in the feldspar grain based on SEM-EDS. This is of no surprise as the relatively small cation (i.e., ionic radius of Mg^{2+} being 0.72 Å as compared to those of Ca^{2+} (1.00 Å), Na^{1+} (1.02 Å), and K^{1+} (1.38 Å)) is incompatible with the feldspar lattice (Nash and Marshall, 1956 [72]) and has only been detected in feldspars formed under special conditions involving supercooling, Mg-bearing feldspar solid solutions being metastable [73].

SEM analysis also reveals de-mixing of dolomite grains upon firing,

leaving behind a Mg-rich porous core that acts as a sink for iron (Fig. 5b, Table 5). The difference in mobility of both alkaline-earth metal ions cannot be explained by the difference in their diffusion coefficient. Considering that the ionic radius of Mg^{2+} is smaller than that of Ca^{2+}, a faster diffusion of the former can be expected, which, indeed, has been observed in the case of Mg and Ca diffusion in calcite at high T [74]. This suggests that a Ca-rich core should remain, which, however, is not the case. Here lattice energies of the alkaline-earth oxides (being −3795 and −3414 kJ/mol for MgO and CaO, respectively) have to be considered, which indicate that MgO is energetically more stable and, therefore less reactive than CaO. In order to elucidate the competing role of Mg^{2+} and Ca^{2+} during the formation of high temperature phases detected in the reaction rim, the molar free energy and enthalpy contributions of individual polyhedral components of the different mineral phases have to be considered. According to the estimation of the free energy of formation of silicate minerals at high T by Chermak and Rimstidt [75], the formation of Ca-rich silicate minerals will generally be more favorable than that of Mg-rich phases of identical composition. The much higher calcium concentration in the reaction rim, can, thus, be explained by the dominance of calcium-rich (alumino)silicates/aluminates. Sintering processes upon firing might add to the observed phenomenon. Indeed, Rodriguez-Navarro et al. [76] observed a significant increase in MgO crystallite size from 15–19 nm at 750 °C to 38–44 nm at 1000 °C due to sintering, rendering Mg less reactive as the firing temperature increases. Note that the scarcity of carbonates limited the amount of newly formed crystalline Ca/Mg-rich silicates/aluminosilicates, which, with the exception of mullite, are below the XRD detection limit.

Finally, it is observed that Mg-rich cores act as a sink for Fe in the brick sample fired at 1100 °C (Table 5). Considering, however, that this behavior is only observed in the black zone, it seems reasonable to assume that it is charge related as the black zone contains almost 10% more Fe^{2+} than the red zone according to XPS. Differences in iron distribution depending on firing atmosphere are not only limited to former carbonate grains (now mainly MgO) but also affects the matrix of bricks fired at 1100 °C, being almost 30% higher in the red zone (oxidative atmosphere) as compared to the black zone (reductive atmosphere) according to SEM-EDS. The lower iron content of the latter could be related to the higher hercynite/hematite ratio in the matrix (the hercynite/hematite ratio of the matrix of the black and red zone being 1.22 and 0.79, respectively), considering that the iron content of hercynite is much lower than that of hematite (the iron content of hercynite and hematite being 33 and 70 wt%, respectively). The differences in iron content of iron-bearing phases in both zones could also be the reason for the accumulation of iron in the Mg-rich cores in the black zone. Overall, these results show that organic matter, a universal soil component, can play an important role (i.e., by influencing the firing conditions) in the mineralogical evolution, particularly in the case of iron compounds, and consequently has a crucial effect on the textural and mechanical characteristics of fired bricks.

5. Conclusions

The comprehensive analysis of bricks offers valuable insights into the mineralogical evolution upon firing, in particular reactions involving the decomposition of carbonate grains and solid state reaction in feldspars. Results also provide clear evidence for the influence of the firing conditions (i.e., reducing or oxidizing atmosphere) on the Fe^{3+}/Fe^{2+} ratio and the iron distribution within matrix and mineral grains, identifying former carbonate grains as sinks for iron under reducing conditions. The ratio Fe^{3+}/Fe^{2+} has an important effect on melt properties and textural characteristics, leading to more advanced vitrification under reducing conditions. These findings have important implication regarding brick fabrication for heritage conservation and new construction especially in Mediterranean countries, as soils commonly contain significant amounts of organic matter, iron compounds, and carbonates.

The overall technical quality of bricks fired ≤ 950 °C fabricated from Alhambra Formation soil is adequate for building purposes and it seems possible to fabricate replacement bricks with hydric and mechanical properties that match those of historic bricks. However, the pore size distribution should be optimized without increasing the open porosity in order to improve brick durability. It should be investigated whether the volume of pores with a diameter > 3 μm could be increased using additives. Recently, Ordieres and Cultrone [31] have shown that coffee grounds might be used to this end.

The addition of KOH leads to an increase in vitrification, but has a negative effect on the hydric properties and mechanical resistance likely due to an increase in porosity and crack formation caused by flocculation of clay minerals during the fabrication process. However, the additive might have limited use to fabricate replacement bricks with low mechanical strength to match the characteristics of low-fired historic ceramics.

Future research should explore whether bricks of suitable technical quality could be obtained at lower T under reducing firing conditions as compared to oxidizing conditions. To this respect the influence of the raw material composition and, in particular the content in iron phases and organic matter have to be considered. This approach could result in a substantial reduction of energy costs and, in combination with the use of organic additives to optimize the pore size distribution, enables the fabrication of more sustainable building bricks for new construction.

Funding

This research was funded by the Spanish Government grant PID2021.125305NB.I00 funded by MCIN/ AEI /10.13039/501100011033 and by ERDF *A Way of Making Europe*, the Unidad de Excelencia "UCE2018-01 - *Ciencia en la Alhambra*" (UGR), the Unidad Cientifica de Excelencia "UCE.PP2016.05″ (UGR), and the Research Group "RNM0179″ (Junta de Andalucia). Funding for open access charge: Universidad de Granada / CBUA

CRediT authorship contribution statement

Kerstin Elert: Conceptualization, Methodology, Investigation, Resources, Writing – Original Draft, Writing – Review & Editing, Visualization, Project administration, Funding acquisition. **Luis Monasterio-Guillot:** Investigation. **Giuseppe Cultrone:** Conceptualization, Methodology, Resources, Writing – Review & Editing, Visualization, Funding acquisition.

Declaration of Competing Interest

The authors declare that they have no known competing financial interests or personal relationships that could have appeared to influence the work reported in this paper.

Acknowledgements

We thank Dr. C. Rodriguez-Navarro for insightfull comments and suggestions. XPS and FESEM analyses were made at the Centro de Instrumentación Científica of the University of Granada.

Appendix A. Supporting information

Supplementary data associated with this article can be found in the online version at doi:10.1016/j.jeurceramsoc.2024.01.062.

References

[1] Y. Yasuda, Discovery of the Yangtze River civilization in China, in: Y. Yasuda (Ed.), Water Civilization. Advances in Asian Human-Environmental Research, Springer, Tokyo, 2013, p. 35.

[2] A., Khan, C. Lemmen, Bricks and urbanism in the Indus Valley rise and decline, arXiv:1303.1426 [physics.hist-ph], 2014, ⟨https://doi.org/10.48550/arXiv.1303.1426⟩.

[3] M. Prevosti, L. Casas, J.F.R. Pérez, B. Fouzai, A. Álvarez, À. Pitarch, Archaeological and archaeomagnetic dating at a site from the ager Tarraconensis (Tarragona, Spain): El Vila-sec Roman, Pottery, J. Archaeol. Sci. 40 (2013) 2686–2701.

[4] M.J. de la Torre, Estudio de los Materiales de Construcción en la Alhambra (Doctoral Thesis), University of Granada, Spain, 1995.

[5] D. Villegas, M. Cámara Pérez, V.J. Compán Cardiel, Análisis estructural de la torre del homenaje de la Alhambra de Granada (España), Inf. De. la Constr. 66 (2014) 1–8.

[6] M. Scolforo, H. Browne, Acquisition and properties of brick for historic structure preservation and rehabilitation. Standards for Preservation and Rehabilitation, ASTM International, West Conshohocken, PA, 1996, pp. 337–347.

[7] A.L. Espinar Moreno, J.M. López Osorio, Restauración de la Torre de Baltasar de la Cruz: una aportación a la recuperación del perfil amurallado de la Alhambra, Cuad. De. Alhambra 40 (2004) 201–220.

[8] K. Elert, G. Cultrone, C. Rodriguez Navarro, E. Sebastián Pardo, Durability of bricks used in the conservation of historic buildings—influence of composition and microstructure, J. Cult. Herit. 4 (2003) 91–99.

[9] E.O. Ontiverios-Ortega, E.Sebastián Pardo, I.V. Espinosa, Deterioration in XI–XIV century arab ramparts (Granada, Spain), Mater. Struct. 32 (1999) 45–51.

[10] H. Justicia Munoz, M.P. Sáez Pérez, J.A. Durán Suárez, M.Á. Villegas Broncano, Study of vernacular building materials used in cultural heritage as a guide for architectural restoration: colegio Máximo de Cartuja. Granada-Spain (19th century), Inf. De. la Constr. 73 (2021) e381.

[11] M.S. Tite, M. Bimson, Glazed steatite: an investigation of the methods of glazing used in ancient Egypt, World Archaeol. 21 (1989) 87–100.

[12] J. Dong, Y. Hu, S. Liu, Q. Li, The transition of alkaline flux of ancient Chinese faience beads (1046–476 BC): a case study on the samples from Pingdingshan, Henan province, Archaeol. Anthropol. Sci. 12 (2020) 1–18.

[13] J.M. Martín Martín, Geología e historia del oro de Granada, Bol. Del. Inst. Geológico Y. Min. De. Esp. 111 (2000) 47–60.

[14] J.M. Martín-García, G. Delgado, J.F. Parraga, J. Bech, R. Delgado, Mineral formation in micaceous Mediterranean red soils of Sierra Nevada, Granada, Spain, Eur. J. Soil Sci. 49 (1998) 253–268.

[15] P.G. Jeffery, D. Hutchison. Chemical Methods of Rock Analysis, Pergamon press, Oxford, 1981.

[16] R.T. Laird, M. Worcester, The inhibition of lime blowing, Trans. Br. Ceram. Soc. 55 (1956) 545–563.

[17] H.M. Rietveld, A profile refinement method for nuclear and magnetic structures, J. Appl. Crystallogr. 2 (1969) 65–71.

[18] J.D. Martín-Ramos, Using XPowder: A Software Package for Powder X-Ray Diffraction Analysis (GR 1001/04. ISBN 84–609-1497–6), 2004.

[19] R.T. Downs, M. Hall-Wallace, The American Mineralogist crystal structure database, Am. Mineral. 88 (2003) 247–250.

[20] UNE-EN 13755, Métodos de ensayo para piedra natural. Determinación de la absorción de agua a presión atmosférica, AENOR, Madrid, 2008.

[21] NORMAL 29/88, Misura dell'indice di asciugamento (Drying index), CNR-ICR, Roma, 1988.

[22] RILEM, Recommended tests to measure the deterioration of stone and to assess the effectiveness of treatment methods, Commision 25-PEM: Protection et Erosion des Monuments, Mater. Struct. 13 (1980) 175–253.

[23] G. Cultrone, E. Sebastián, K. Elert, M.J. De la Torre, O. Cazalla, C. Rodriguez–Navarro, Influence of mineralogy and firing temperature on the porosity of bricks, J. Eur. Ceram. Soc. 24 (2004) 547–564.

[24] UNE-EN 828Adhesivos. Mojabilidad. Determinación por medida del ángulo de contacto y de la tensión superficial crítica de la superficie sólida (Adhesives - Wettability - Determination by measurement of contact angle and surface free energy of solid surface), AENOR, Madrid, 2013, p. 3013.

[25] UNE-EN 1015-11:2020, Métodos de ensayo de los morteros para albañilería. Parte 11: Determinación de la resistencia a flexión y a compresión del mortero endurecido (Methods of test for mortar for masonry - Part 11: Determination of flexural and compressive strength of hardened mortar), AENOR, Madrid, 2020.

[26] ASTM D2845, Standard Test Method for Laboratory Determination of Pulse Velocities and Ultrasonic Elastic Constants of Rock, ASTM Int., West Conshohocken, PA, 2000.

[27] E.M. Pérez-Monserrat, L. Maritan, E. Garbin, G. Cultrone, Production technologies of ancient bricks from Padua, Italy: changing colors and resistance over time, Minerals 11 (2021) 744.

[28] R. Kreimeyer, Some notes on the firing colour of clay bricks, Appl. Clay Sci. 2 (1987) 175–183.

[29] C. Rathossi, Y. Pontikes, Effect of firing temperature and atmosphere on ceramics made of NW Peloponnese clay sediments. Part I: reaction paths, crystalline phases, microstructure and colour, J. Eur. Ceram. Soc. 30 (2010) 1841–1851.

[30] L. Nodari, E. Marcuz, L. Maritan, C. Mazzoli, U. Russo, Hematite nucleation and growth in the firing of carbonate-rich clay for pottery production, J. Eur. Ceram. Soc. 27 (2007) 4665–4673.

[31] R. Ordieres, G. Cultrone, Technical quality of solid bricks made using clayey earth with added coffee grounds and fly ash, Constr. Build. Mater. 341 (2022) 127757.

[32] Å.L. Lyne, P. Redelius, M. Collin, B. Birgisson, Characterization of stripping properties of stone material in asphalt, Mater. Struct. 46 (2013) 47–61.

[33] Y. Maniatis, M.S. Tite, Technological examination of neolithic-bronze age pottery from central and southeast Europe and from the near East, J. Archaeol. Sci. 8 (1981) 59–76.

[34] V. Fuertes, J.J. Reinosa, J.F. Fernández, E. Enríquez, Engineered feldspar-based ceramics: a review of their potential in ceramic industry, J. Eur. Ceram. Soc. 42 (2022) 307–326.

[35] J. Parras, C. Sánchez Jiménez, M. Rodas, F.J. Luque, Ceramic applications of Middle Ordovician shales from central Spain, Appl. Clay Sci. 11 (1996) 25–41.

[36] E. Rodríguez, G.A. Castillo, J. Contreras, R. Puente-Ornelas, J.A. Aguilar-Martínez, L. García, C. Gomez, Hercynite and magnesium aluminate spinels acting as a ceramic bonding in an electrofused MgO–CaZrO3 refractory brick for the cement industry, Ceram. Int. 38 (2012) 6769–6775.

[37] L. Maritan, L. Nodari, C. Mazzoli, A. Milano, U. Russo, Influence of firing conditions on ceramic products: experimental study on clay rich in organic matter, Appl. Clay Sci. 31 (2006) 1–15.

[38] J.C. Cerdeño del Castillo, R.D. Rubio, J.O. Sánchez, A.P. Lorenzo, J.V. Vélez, Manual de patologías de las piezas cerámicas para la construcción, AITEMIN,, Toledo, 2000.

[39] C. Rodriguez Navarro, G. Cultrone, A. Sánchez Navas, E. Sebastián, TEM study of mullite growth after muscovite breakdown, Am. Mineral. 88 (2003) 713–724.

[40] T. Yamashita, P. Hayes, Analysis of XPS spectra of Fe2+ and Fe3+ ions in oxide materials, Appl. Surf. Sci. 254 (2008) 2441–2449.

[41] H. Schneider, H. Rager, Iron incorporation in mullite, Ceram. Int. 12 (1986) 117–125.

[42] A.F. Plante, M. Pernes, C. Chenu, Changes in clay-associated organic matter quality in a C depletion sequence as measured by differential thermal analyses, Geoderma 129 (2005) 186–199.

[43] B.A. Schumacher, Methods for the Determination of Total Organic Carbon (TOC) in Soils And Sediments, US Environmental Protection Agency, Las Vegas, 2002.

[44] G. Cultrone, E. Sebastián, Fly ash addition in clayey materials to improve the quality of solid bricks, Constr. Build. Mater. 23 (2009) 1178–1184.

[45] C. Coletti, G. Cultrone, L. Maritan, C. Mazzoli, Combined multi-analytical approach for study of pore system in bricks: how much porosity is there? Mater. Charact. 121 (2016) 82–92.

[46] ASTM C62 – 23, Standard Specification for Building Brick (Solid Masonry Units Made from Clay or Shale), ASTM Int., West Conshohocken, PA, 2023.

[47] S. Iglauer, C.H. Pentland, A. Busch, CO_2 wettability of seal and reservoir rocks and the implications for carbon geo-sequestration, Water Resour. Res. 51 (2015) 729–774.

[48] S. Noor-E-Khuda, F. Albermani, Mechanical properties of clay masonry units: destructive and ultrasonic testing, Constr. Build. Mater. 219 (2019) 111–120.

[49] D.N. Nkayem, J.A. Mbey, B.K. Diffo, D. Njopwouo, Preliminary study on the use of corn cob as pore forming agent in lightweight clay bricks: Physical and mechanical features, J. Build. Eng. 5 (2016) 254–259.

[50] Pliego RL-88, Recepción de los ladrillos cerámicos Orden MOPU, (B.O.E. 1988.08.03), Madrid, 1988.

[51] S.R. Koroth, D. Feldman, P. Fazio, Development of new durability index for clay bricks, J. Archit. Eng. 4 (1998) 87–93.

[52] K.J. Krakowiak, P.B. Lourenço, F.J. Ulm, Multitechnique investigation of extruded clay brick microstructure, J. Am. Ceram. Soc. 94 (2011) 3012–3022.

[53] A. Viani, G. Cultrone, K. Sotiriadis, R. Ševčík, P. Šašek, The use of mineralogical indicators for the assessment of firing temperature in fired-clay bodies, Appl. Clay Sci. 163 (2018) 108–118.

[54] J.S. Johnson, J. Clark, S. Miller-Antonio, D. Robins, M.B. Schiffer, J.M. Skibo, Effects of firing temperature on the fate of naturally occurring organic matter in clays, J. Archaeol. Sci. 15 (1988) 403–414.

[55] T. Osugi, S. Sukenaga, Y. Inatomi, Y. Gonda, N. Saito, K. Nakashima, Effect of oxidation state of iron ions on the viscosity of alkali silicate melts, ISIJ Int 53 (2013) 185–190.

[56] D. Di Genova, J. Vasseur, K.U. Hess, D.R. Neuville, D.B. Dingwell, Effect of oxygen fugacity on the glass transition, viscosity and structure of silica-and iron-rich magmatic melts, J. Non-Cryst. Solids 470 (2017) 78–85.

[57] B.O. Mysen, D. Virgo, E.R. Neumann, F.A. Seifert, Redox equilibria and the structural states of ferric and ferrous iron in melts in the system $CaO–MgO–Al_2O_3–SiO_2–Fe–O$;: relationships between redox equilibria, melt structure and liquidus phase equilibria, Am. Mineral. 70 (1985) 317–331.

[58] B. Lubelli, R.P. van Hees, Desalination of masonry structures: Fine tuning of pore size distribution of poultices to substrate properties, J. Cult. Herit. 11 (2010) 10–18.

[59] P. Lopez-Arce, J. Garcia-Guinea, Weathering traces in ancient bricks from historic buildings, Build. Environ. 40 (2005) 929–941.

[60] D. Medjelekh, A. Kenai, S. Claude, S. Ginestet, G. Escadeillas, Multi-technique characterization of ancient materials as part of an eco-renovation of historic centres, case of Cahors centre in France, Constr. Build. Mater. 250 (2020) 118894.

[61] A. Al-Omari, S. Khattab, Characterization of building materials used in the construction of historical Al-Omariya mosque minaret in Mosul's old city, Iraq, J. Build. Eng. 33 (2021) 101645.

[62] M. Maage, Frost resistance and pore size distribution in bricks, Mater. Struct. 17 (1984) 345–350.

[63] Y.M. Mowafy, G.E. Bauer, F.H. Sakeb, Treatment of expansive soils: a laboratory study, Transp. Res. Rec. 1032 (1985) 34–39.

[64] M.J. Scolforo, H. Browne, Acquisition and properties of brick for historic structure preservation and rehabilitation, ASTM Special Technical Publication 1258, ASTM Int, West Conshohocken, PA, 1996, pp. 337–352.

[65] F. Fernandes, P.B. Lourenço, Evaluation of the compressive strength of ancient clay bricks using microdrilling, J. Mater. Civ. Eng. 19 (2007) 791–800.

[66] P. Matysek, M. Witkowski, A comparative study on the compressive strength of bricks from different historical periods, Int. J. Archit. Herit. 10 (2016) 396–405.

[67] A.B. Ramos Gavilán, M.A. Rodríguez Esteban, M.N. Antón Iglesias, M.P. Sáez Perez, M.S. Camino Olea, J. Caballero Valdizán, Experimental study of the mechanical behaviour of bricks from 19th and 20th century buildings in the province of Zamora (Spain), Infrastructures 3 (2018) 38.
[68] B. Graue, S. Siegesmund, B. Middendorf, Quality assessment of replacement stones for the Cologne Cathedral: mineralogical and petrophysical requirements, Environ. Earth Sci. 63 (2011) 1799–1822.
[69] J.R. Goldsmith, F. Laves, The microcline-sanidine stability relations, Geochim. Cosmochim. Acta 5 (1954) 1–19.
[70] G. Cultrone, C. Rodriguez-Navarro, E. Sebastian, O. Cazalla, M.J. De La Torre, Carbonate and silicate phase reactions during ceramic firing, Eur. J. Mineral. 13 (2001) 621–634.
[71] P. Ballato, G. Cruciani, M.C. Dalconi, B. Fabbri, M. Macchiarola, Mineralogical study of historical bricks from the Great Palace of the Byzantine Emperors in Istanbul based on powder X-ray diffraction data, Eur. J. Mineral. 17 (2005) 777–784.
[72] V.E. Nash, C.E. Marshall, The surface reactions of silicate minerals. Part I, The reactions of feldspar surfaces with acidic solutions, University of Missouri, College of Agriculture, 1956, p. 36.
[73] R.S. Zeng, $CaMgSi_3O8$, the MacKenzie's molecule, a possible indicator of supercooling, Bull. De. Minéralogie 108 (1985) 713–718.
[74] D.K. Fisler, R.T. Cygan, Diffusion of Ca and Mg in calcite, Am. Mineral. 84 (1999) 1392–1399.
[75] J.A. Chermak, J.D. Rimstidt, Estimating the free energy of formation of silicate minerals at high temperatures from the sum of polyhedral contributions, Am. Mineral. 75 (1990) 1376–1380.
[76] C. Rodriguez-Navarro, K. Kudlacz, E. Ruiz-Agudo, The mechanism of thermal decomposition of dolomite: new insights from 2D-XRD and TEM analyses, Am. Mineral. 97 (2012) 38–51.